NANO LETTERS

pubs.acs.org/NanoLett Letter

Enhancing Perpendicular Magnetic Anisotropy in Garnet Ferrimagnet by Interfacing with Few-Layer WTe_2

Guanzhong Wu,* Dongying Wang, Nishchhal Verma, Rahul Rao, Yang Cheng, Side Guo, Guixin Cao, Kenji Watanabe, Takashi Taniguchi, Chun Ning Lau, Fengyuan Yang, Mohit Randeria, Marc Bockrath, and P. Chris Hammel

Cite This: *Nano Lett.* 2022, 22, 1115–1121 Read Online

ACCESS | Metrics & More | Article Recommendations | Supporting Information

ABSTRACT: Engineering magnetic anisotropy in a ferro- or ferrimagnetic (FM) thin film is crucial in a spintronic device. One way to modify the magnetic anisotropy is through the surface of the FM thin film. Here, we report the emergence of a perpendicular magnetic anisotropy (PMA) induced by interfacial interactions in a heterostructure comprised of a garnet ferrimagnet, $Y_3Fe_5O_{12}$ (YIG), and a low-symmetry, high spin-orbit coupling (SOC) transition metal dichalcogenide, WTe_2. At the same time, we also observed an enhancement in Gilbert damping in the WTe_2-covered YIG area. Both the magnitude of interface-induced PMA and the Gilbert damping enhancement have no observable WTe_2 thickness dependence down to a single quadruple layer, indicating that the interfacial interaction plays a critical role. The ability of WTe_2 to enhance the PMA in FM thin film, combined with its previously reported capability to generate out-of-plane damping like spin torque, makes it desirable for magnetic memory applications.

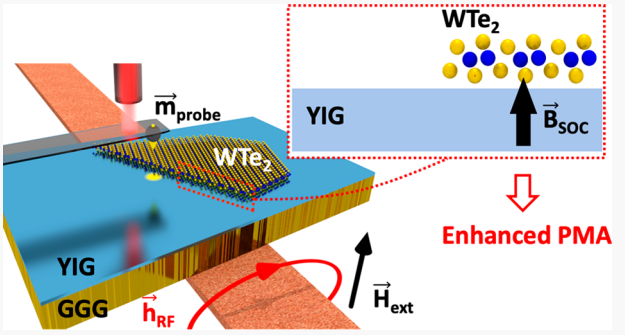

KEYWORDS: *perpendicular magnetic anisotropy, magnetic resonance force microscope, transition metal dichalcogenides, ferrimagnetic insulator*

Perpendicular magnetic anisotropy (PMA) in a ferromagnetic thin film is of great interest in spintronics research and applications. Ferromagnetic nanoelements with PMA overcome their shape anisotropy, greatly ease the memory cell size reduction, and improve memory retention. These exceptional properties, improving the performance of magnetic devices, make PMA highly desirable for magnetic memory applications. PMA becomes even more important in the recent development of solid-state magnetic random-access memory (MRAM) since it allows MRAM to have a lower switching current and a faster switching speed compared to in-plane magnetized materials.[1,2]

Magnetic storage devices generally rely on metallic magnetic materials due to their robust electrical response. Interfacial magnetic anisotropy plays a critical role in generating PMA in metallic ferromagnets. When interfacing with a nonmagnetic material (NM), the electron orbital angular momentum of the magnetic ions at the ferromagnet surface will be modified, in some cases enabling strong covalent bonding, resulting in distinct magnetic properties compared to the single layer.[3−6] However, spintronics devices made of metallic magnetic materials are inherently energy consumptive due to resistive losses. Recently, complex oxide ferro- or ferrimagnet insulators (FMI) have attracted substantial interest due to their ability to transport spin excitations with low dissipation.[7] Inducing PMA in FMIs naturally becomes an important topic both for scientific and technological reasons. Several successful routes to achieving PMA in FMIs have been reported using bulk intrinsic anisotropy[8] or lattice strain.[9−12] However, in most experiments, the sign of the resulting interfacial anisotropy in FMI/NM heterostructures is such as to enhance the easy-plane anisotropy.[13−15] Only one recent experiment has shown the possibility of generating interfacial PMA, and this was attributed to topological surface states.[16] Nevertheless, these results demonstrate the possibility of controlling magnetic anisotropy through interfacial interactions in FMI/NM heterostructures. Here, we report a study on YIG/WTe_2/hBN heterostructures, which shows that, when interfacing with a low symmetry nonmagnetic van der Waals material, WTe_2, an additional interface-induced PMA (iPMA) term emerges in the magnetic anisotropy of the YIG thin film. The absence of topological surface states at room temperature in WTe_2[17,18]

Received: November 3, 2021
Revised: January 22, 2022
Published: January 31, 2022

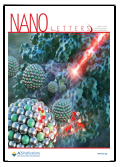

https://doi.org/10.1021/acs.nanolett.1c04237
Nano Lett. 2022, 22, 1115−1121

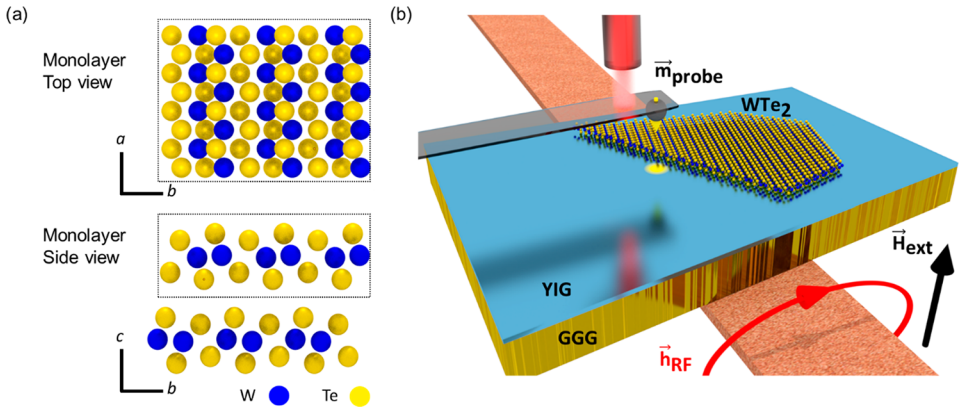

Figure 1. Crystal structure of WTe_2 and sample schematic. (a) Crystal lattice structure of WTe_2 viewed from the top along the *c*-axis and looking from the side along the *a*-axis. The black dashed box in the side view indicates a monolayer of WTe_2. (b) Schematic of the ferromagnetic resonance force microscope. RF excitation is generated by a stripline underneath the sample, where the hBN encapsulation is not shown. The region of localized mode is shown as a yellow dot adjacent to the WTe_2 flake, and the probe magnetic moment is shown as a yellow arrow on the particle. The cantilever oscillation is detected by a fiber laser interferometer.

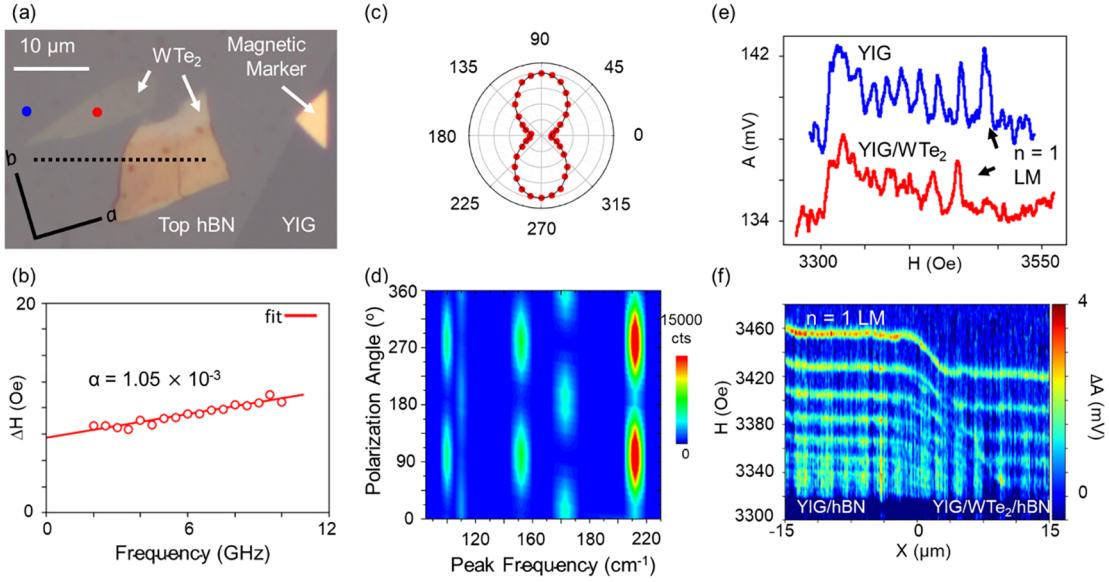

Figure 2. FMRFM and Raman measurement data. (a) An optical micrograph of the YIG/WTe_2/hBN heterostructure under study. The WTe_2 crystal *a* and *b* axes are labeled. (b) Broadband FMR measurement of the frequency-dependent line width of the YIG thin film. The measurement is done on the same piece of YIG used to make the sample shown in Figure 1b. (c) Polar plot of the 212 cm^{-1} peak Raman intensity. The angle denotes the relative angle between the measurement laser polarization and the WTe_2 *a* axis. (d) 2D intensity plot showing Raman peak intensities versus polarization angle. (e) FMRFM spectra, one over the YIG/hBN region (blue line) and the second over the YIG/WTe_2/hBN region (red line); these locations are indicated by the blue and red dots in panel a, respectively. (f) Color plot of field-dependence FMRFM scans as a function of position along the trace indicated by the black dashed line in panel a. A constant background is subtracted to show only the signal from several LM resonances.

forces us to seek an explanation for our observation of enhanced PMA that is distinct from that proposed for topological insulator/YIG bilayers.[16] We, therefore, turn to an analysis of the broken symmetries in WTe_2. We point out that low symmetry WTe_2 has recently shown the capability of generating both in-plane and out-of-plane spin polarization in charge-spin conversion experiments.[19−22] It also enables field-free switching of PMA magnetic material, which eases the application of PMA materials in MRAM applications.[23−25]

Ferrimagnetic insulator YIG is of significant research interest in spintronics due to its exceptionally low Gilbert damping,[26] which describes the relaxation rate of magnetization precession, and 1T′-WTe_2 is a semimetallic transition metal dichalcogenide (TMD) layered material with strong SOC.[27,28] The crystal structure of 1T′-WTe_2 lacks 2-fold rotational symmetry about the *c*-axis (Figure 1a). The only symmetry in the WTe_2 crystal lattice *ab* plane is the mirror symmetry about the *bc* plane.[29] This unique symmetry breaking allows out-of-plane damping-like torque to be generated,[30,31] enabling efficient switching of the out-of-plane magnetization of the adjacent magnetic material.[24]

A 20 nm thick YIG thin film used in our experiment is epitaxially grown on the (111)-oriented $Gd_3Ga_5O_{12}$ (GGG) substrate by off-axis sputtering.[32] WTe_2 flakes are then mechanically exfoliated from a flux-grown crystal and dry transferred onto the clean top YIG surface without touching any other substances. This whole process is carried out in an Ar-filled glovebox with <0.1 ppm of H_2O and O_2 to protect the

https://doi.org/10.1021/acs.nanolett.1c04237
Nano Lett. 2022, 22, 1115−1121

flakes from degradation and ensure the cleanliness of the YIG/WTe_2 interface. We employ hexagonal boron nitride (hBN) encapsulation to protect the WTe_2 flakes from oxidation after being removed from the glovebox. We make two samples and focus on the data taken from sample 1 in the main text. The raw data taken from sample 2 can be found in Figure S2.

Figure 2a shows an optical image of sample 1. Due to the small lateral size of the exfoliated WTe_2 and hBN flakes having length scales of 10 μm, we use a home-built ferromagnetic resonance force microscope (FMRFM) to measure the local ferromagnetic resonance (FMR) signal. FMRFM is a sensitive technique to detect the local magnetic properties with high spatial and spectral resolution.[33] In our FMRFM, the external magnetic field $\vec{H}_{ext}$ is aligned perpendicular to the sample plane. The cantilever tip holds a high coercivity $SmCo_5$ magnetic particle, whose moment is magnetized in the direction opposite to $\vec{H}_{ext}$ to create a magnetic field well. The field well supports a set of localized standing spin wave modes (LMs). During the measurement, we excite spin precession uniformly by a stripline underneath the sample at a fixed RF frequency (2 GHz) and sweep the magnetic field. The resonance of each LM generates a stray field, which can then be detected by the $SmCo_5$ magnetic particle attached to the cantilever through their magnetic dipole−dipole interaction (Figure 1b). During the measurement, we keep the probe-to-sample separation around 4 μm. The operation of FMRFM is described in detail in refs 34−36. For reference, we separate a region of YIG that does not contain WTe_2/hBN heterostructures and measure its Gilbert damping using broadband FMR. To eliminate two-magnon scattering, we perform broadband FMR in the out-of-plane field geometry. The FMR line width as a function of frequency measured on bare YIG (sample 1) shows a linear dependence (Figure 2b), from which we can extract the Gilbert damping of bare YIG $\alpha_{YIG} = 1.05 \times 10^{-3}$. We also confirm that the WTe_2 used in the experiment is indeed the 1T′ phase through polarized Raman measurements. The polarization angle dependence of the Raman peak at 212 cm^{-1} (the spectrum is shown in Figure S4) exhibits minimum intensity when the excitation laser polarization is along the crystallographic a axis of WTe_2[37] as shown by the polar plot in Figure 2c and Raman intensity plot in Figure 2d.

We find the position of the YIG/WTe_2/hBN heterostructure with the assistance of magnetic alignment markers (Figure 2a). Figure 2e shows two raw FMRFM scans taken in the region of YIG/hBN and YIG/WTe_2/hBN, indicated by the blue and the red dot in Figure 2a, respectively, which reveals the change in FMRFM spectra at two different locations. Here we focus on the n = 1 LM because it has a mode radius of around 1 μm and gives the highest spatial resolution. Higher-order modes have an increasing mode radius and, therefore, detect less localized magnetic properties. This is the reason why the quasi-uniform mode at ∼3325 Oe does not show an obvious change in resonance field or signal amplitude. We further take a line scan across the edge of the WTe_2 flake (Figure 2f) to resolve the spatial evolution of FMRFM spectra. The line scan in Figure 2f (along the dashed line shown in Figure 2a) shows three main features: first, the magnitude of the LM resonance signal is reduced in the YIG/WTe_2/hBN region compared to the YIG/hBN region; second, the LM resonance field for all LMs is decreased by ∼40 Oe in the YIG/WTe_2/hBN region; third, the LMs show complex splitting and crossing when the probe is close to the boundary ($-5\ \mu m < X < 10\ \mu m$).

In the following, we will explain the origin of the three observed effects using spin pumping and magnetic anisotropy. The first effect, i.e., signal reduction in the YIG/WTe_2/hBN area relative to the YIG/hBN area, is the result of enhanced relaxation due to spin pumping from YIG to WTe_2.[38] The n = 1 LM resonance signal amplitude ΔA is inversely proportional to the square of Gilbert damping, α^2. We determine the Gilbert damping constant α for YIG/WTe_2/hBN using $\alpha_{YIG/WTe_2/hBN} = \alpha_{YIG/hBN} \times \sqrt{\Delta A_{YIG/hBN}/\Delta A_{YIG/WTe_2/hBN}}$ (see ref 39), where $\alpha_{YIG/hBN}$ is assumed to be the same as $\alpha_{YIG} = 1.05 \times 10^{-3}$ due to the low SOC and insulating character of hBN. The second effect is the decrease of n = 1 LM resonance field $H_{r,1}$ by ∼40 Oe. The third effect is splitting and crossing of complex modes in the region $-5\ \mu m < X < 10\ \mu m$. The second and the third effects are due to an abrupt change of uniaxial anisotropy across the boundary separating the YIG/WTe_2/hBN and YIG/hBN regions.[15] Here, the uniaxial anisotropy refers to the magnetic free energy depending on the angle between magnetization and sample normal $\mathcal{F}_u = -K_u \boldsymbol{m}_z^2$, where $\boldsymbol{m}_z$ is the component of magnetization unit vector in the direction normal to sample plane, and K_u is the uniaxial anisotropy constant specific to sample and depends on the total interaction in the sample. When K_u is positive, $\mathcal{F}_u$ is called to be of PMA type; on the other hand, if K_u is negative, $\mathcal{F}_u$ is called to be of easy-plane type. This uniaxial anisotropy will lead to an effective uniaxial magnetic field $\boldsymbol{H}_u = -\partial \mathcal{F}_u / \partial \boldsymbol{M}$, where $\boldsymbol{M}$ is the magnetization. Therefore, a change in K_u can modify the resonance field in a FMR measurement. In FMRFM spatial mapping, an abrupt change in K_u spatially could disturb the LM and lead to mode splitting and crossing as described in ref 15. Moreover, in striking contrast to the previously studied YIG/Au interface,[15] which results in a 32 Oe increase of $H_{r,1}$ due to the enhanced easy-plane anisotropy, the observed decrease of $H_{r,1}$ indicates that the WTe_2 overlayer induces an iPMA in YIG. We note that the magnitude of the shift in $H_{r,1}$ is comparable to the easy-plane anisotropy induced by a heavy metal[15,40] or the iPMA generated by topological surface state[16] on garnet ferrimagnetic material.

In order to probe the global effect of a WTe_2 overlayer on YIG, we spatially map $H_{r,1}$ using the n = 1 LM. Figure 3a presents an optical image of WTe_2 flakes on a Si/SiO_2 (285 nm) substrate, where different colors of WTe_2 flakes indicate different WTe_2 thicknesses. Figure 3b,c shows spatial maps of magnetic properties in the region enclosed by the black dashed rectangle in Figure 3a. We acquire the maps using the procedure described in ref 39, i.e., simultaneously measuring the spatial variation of the magnetic anisotropy and Gilbert damping using the n = 1 LM resonance field $H_{r,1}$ and signal amplitude ΔA. The entire WTe_2-covered area shows uniformly lowered $H_{r,1}$ and increased Gilbert damping relative to the area without WTe_2. In Figure 3c, despite the not great signal-to-noise ratio in the damping imaging, there is a clear Gilbert damping enhancement in the WTe_2-covered area. The averaged Gilbert damping of YIG in the WTe_2-covered area is $\bar{\alpha}_{YIG/WTe_2/hBN} \approx 1.30 \times 10^{-3}$, about 24% higher than α_{YIG}. We note that, due to the slight relative tilting of the scan plane and the sample plane, there is a color shift in Figure 3b that might conceal the contrast difference in different WTe_2 thickness regions. Therefore, to study the WTe_2 thickness dependence, we will show fine line scans across edges of flakes

https://doi.org/10.1021/acs.nanolett.1c04237
Nano Lett. 2022, 22, 1115−1121

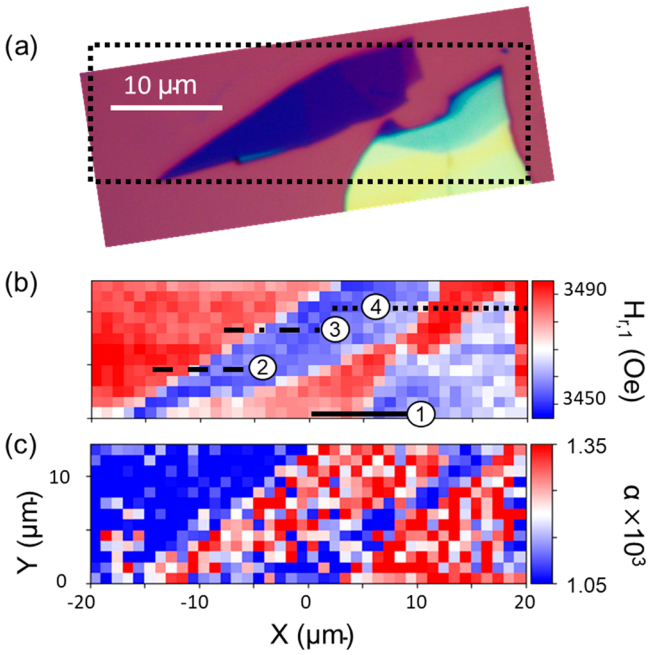

Figure 3. Two-dimensional FMRFM scan resolving the spatial variation of magnetic anisotropy and Gilbert damping. (a) Optical micrograph showing the color contrast of different thickness WTe_2 flakes (ranging from 4.7 to 44.8 nm) on Si/SiO_2 (300 nm). The black dashed box outlines the FMRFM scanned area for 2D mapping. (b) 2D map of the n = 1 LM resonance field. The dashed lines labeled 1−4 correspond to the four line scans shown in Figure S1a−d. (c) 2D mapping of the Gilbert damping extracted from the n = 1 LM resonance peak amplitude.

having different WTe_2 thicknesses. Next, we want to understand what gives rise to the PMA in WTe_2/YIG. We rule out the effect induced by a modification of the gyromagnetic ratio by showing the resonance field shift across the WTe_2 edge does not depend on RF excitation frequency (see Figure S3). We also exclude a strain-induced effect given the absence of an epitaxial relation and the weakness of the van der Waals interaction between YIG and WTe_2. We further note that we can ignore the role of topological surface states[16] in our analysis; they are not relevant for our room temperature experiment since WTe_2 is a topological Weyl semimetal only below 100 K.[17,18]

We show how an analysis based on symmetry and the nature of the interfacial SOC, generalizing the theory in ref 41, gives insight into the PMA observed in our experiment. This will also help us understand why the easy-axis anisotropy we observe in WTe_2/YIG is so different from the results of refs 13 and 15 on YIG interfaces with a dozen different metallic and semiconducting materials, all of which exhibit interface-induced easy-plane anisotropy, as is predicted by theory.[41] YIG is a ferrimagnetic Mott insulator, with two inequivalent Fe-sites coupled via antiferromagnetic (AFM) superexchange interactions. We focus on how interfacial SOC impacts AFM superexchange in YIG and show that it leads to a very specific form of the magnetic anisotropy that is governed by the direction of the effective **B**-field (see Supporting Information for details).

Before turning to WTe_2/YIG, it is useful to first consider the simpler case when the only broken symmetry is the mirror plane defined by the interface. The abrupt change in lattice potential then results in an effective electric field that points normal to the interface, which in turn leads to an effective magnetic field in the rest frame of the electron that couples to its spin. Since the **E**-field points normal to the interfacial plane in which the electron moves, the resulting **B**-field arising from SOC lies within the interfacial plane. As we show in the Supporting Information, this leads to a SOC-induced correction to AFM superexchange that necessarily leads to an easy-plane anisotropy.

In the case of WTe_2/YIG, however, when there are additional broken symmetries, the interface breaks inversion symmetry; also, the crystal structure of WTe_2 itself breaks in-plane inversion symmetry. The electric field is now no longer normal to the interface, and the effective **B**-field arising from SOC necessarily has an out-of-plane component, as shown in Figure S5b. Thus, we see why the lower symmetry of WTe_2/YIG can naturally result in an easy-axis or perpendicular magnetic anisotropy (PMA); see Supporting Information for details.

We note that the lack of 2-fold rotational symmetry in the *ab* plane in WTe_2 that plays a critical role in our understanding of PMA in WTe_2/YIG has also been pointed out to be crucial for the out-of-plane damping-like torque in WTe_2/Permalloy.[30] We note, however, that the out-of-plane damping-like torque necessarily involves current flow in WTe_2, while the PMA is an equilibrium property of the system independent of current flow.

We further demonstrate the interfacial origin of the observed effect by studying the influence of WTe_2 thickness. We show four line scans, labeled in Figure 3b, across the edges of WTe_2 with different thicknesses, ranging from 4.7 to 44.8 nm. From these four line scans, we extract the n = 1 LM resonance field $H_{r,1}$ and the n = 1 LM resonance signal amplitude ΔA. Figure S1a−d shows the evolution of $H_{r,1}$ and ΔA along the traces labeled correspondingly. The thickness of WTe_2 at each measurement location is later measured using atomic force microscopy. From these line scans, we choose the regions where the probe is far away from the edge of WTe_2 so that the magnetic properties are uniform to obtain spatial averages of $H_{r,1}$ and ΔA, which are denoted $\bar{H}_{r,1,\mathrm{YIG/hBN}}$ and $\overline{\Delta A}_{\mathrm{YIG/hBN}}$ in the YIG/hBN region, and $\bar{H}_{r,1,\mathrm{YIG/WTe_2/hBN}}$ and $\overline{\Delta A}_{\mathrm{YIG/WTe_2/hBN}}$ in the YIG/WTe_2/hBN region, respectively. We further extract the n = 1 LM resonance field difference between two regions using $\Delta H_{r,1} = \bar{H}_{r,1,\mathrm{YIG/hBN}} - \bar{H}_{r,1,\mathrm{YIG/WTe_2/hBN}}$, as well as the Gilbert damping difference using $\Delta\alpha = \alpha_{\mathrm{YIG}} \times \left(\sqrt{\overline{\Delta A}_{\mathrm{YIG/hBN}}/\overline{\Delta A}_{\mathrm{YIG/WTe_2/hBN}}} - 1\right)$ as a function of the WTe_2 thickness. We note that the hBN overlayer does not change the Gilbert damping in YIG. The summarized results containing the data from both sample 1 and sample 2 are shown in Figure 4a,b. Raw data from sample 2 can be found in Figure S2. The thinnest WTe_2 acquired in the experiment is 3.2 nm from sample 2, which is approximately the thickness of a quadruple-layer WTe_2.

Figure 4a,b indicates that both $\Delta H_{r,1}$ and $\Delta\alpha$ have almost no WTe_2 thickness dependence. There is a small sample-to-sample variation, possibly due to different YIG/WTe_2 interfacial quality. The change of n = 1 LM resonance field, $\Delta H_{r,1}$, is as large as ∼38 Oe even when the WTe_2 thickness approaches the quadruple-layer thickness. This indicates that the modification of magnetic anisotropy is due to the YIG/WTe_2 interfacial interaction, with no bulk contribution. For the increase of Gilbert damping $\Delta\alpha$, no obvious thickness

https://doi.org/10.1021/acs.nanolett.1c04237
Nano Lett. 2022, 22, 1115−1121

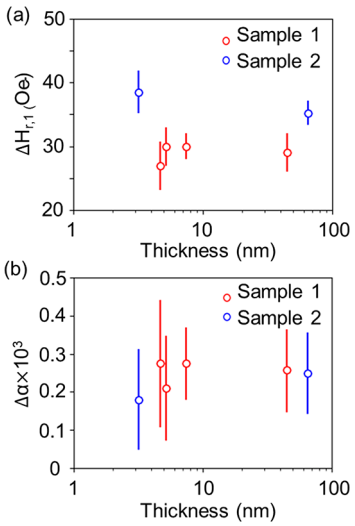

Figure 4. WTe_2 thickness dependence of the resonance field and damping enhancement. (a) $H_{r,1}$ in the YIG/hBN and YIG/WTe_2/hBN regions are averaged, respectively, to get $\bar{H}_{r,1,YIG}$ and $\bar{H}_{r,1,YIG/WTe_2}$, and $\Delta H_{r,1} = \bar{H}_{r,1,YIG} - \bar{H}_{r,1,YIG/WTe_2}$. (b) $\Delta\alpha$ as a function of WTe_2 thickness; $\Delta\alpha = \alpha_{YIG/WTe_2} - \alpha_{YIG}$, where α_{YIG} is the Gilbert damping of bare YIG measured using broadband FMR for each sample, and $\alpha_{YIG/WTe_2} = \alpha_{YIG} \times (\sqrt{\overline{\Delta A}_{YIG/hBN}/\overline{\Delta A}_{YIG/WTe_2/hBN}})$.

dependence is observed when comparing the data from the same sample. In sample 2, the Gilbert damping enhancement due to the quadruple-layer WTe_2 has almost the same value as the 50 nm thick WTe_2 flake, indicating that no thickness dependence of spin pumping can be resolved from our measurement. There are two possible interpretations of these results. First, if the spin current injected into WTe_2 is mainly relaxed due to spin relaxation in the bulk, then the experimental result is a demonstration of ultrashort spin diffusion length along the *c* axis,[38] smaller or comparable to the thinnest WTe_2 flake (3.2 nm), employed in this experiment. It is much smaller than the 8 nm spin diffusion length in the in-plane direction measured using the inverse spin Hall effect.[22] Note that, due to the change in mobility and the metal−insulator transition in few-layer WTe_2 when its thickness reduces,[42] the spin diffusion length approximated here could be inaccurate. Alternatively, it is possible that the spin relaxation is primarily due to the interfacial SOC induced by inversion symmetry breaking at the interface and in the WTe_2 crystal lattice. In this case, the Gilbert damping enhancement will have no WTe_2 thickness dependence.

In conclusion, we have shown that the YIG/WTe_2 interface plays a critical role in both interfacial magnetic anisotropy and spin relaxation, making WTe_2 a promising material in magnetic memory applications. Combining the iPMA created by WTe_2 with the out-of-plane spin-orbit torque generated by flowing a charge current along the *a* axis of WTe_2, one can possibly achieve field-free switching of a PMA magnetic cell for magnetic memory applications. It will improve the scalability, reduce the power consumption, and increase the operation speed of magnetic solid-state devices. Our result reveals new possibilities in selecting materials and designing spintronic devices. For example, one can consider other materials with low lattice symmetry and strong SOC to induce larger PMA type interfacial anisotropy in FMIs. To achieve a fully PMA material, one could utilize thinner FMIs to magnify the role of iPMA. Moreover, interfacial SOC also plays an important role in generating topologically protected magnetic textures in the FMIs.[43] These findings will motivate further research to reveal the fundamental physics arising at the interface between FMIs and nonmagnetic materials.

Methods. *Sample Fabrication.* Our YIG/WTe_2/hBN heterostructure was prepared by means of dry transfer and stacking.[44] hBN crystals were mechanically exfoliated under ambient conditions onto SiO_2/Si substrates (285 nm thick SiO_2), and 20−40 nm thick hBN flakes were identified under an optical microscope and used for the capping layer for the stack. The hBN was picked up using a polymer-based dry transfer technique and then moved into an Ar-filled glovebox with oxygen and water levels below 0.1 ppm. Flux-grown WTe_2 crystals[45] were exfoliated inside the glovebox, and flakes with different thicknesses were optically identified and quickly picked up with the capping hBN layer, then transferred to the YIG substrate. Finally, we removed the fully encapsulated sample from the glovebox and performed the e-beam lithography and metallization (Ni/Au) step for alignment in our ferromagnetic resonance force microscope (FMRFM).

Polarized Raman Measurement. Polarized Raman spectra from the WTe_2 sample were collected using a 633 nm excitation wavelength in an inVia Renishaw Raman microscope. The sample was loaded onto the microscope stage and positioned in such a way that the long edge of the flake was aligned parallel to the laser polarization (θ = 0°). In this configuration, the incident illumination is polarized vertically coming out of the laser and is aligned with the long axis of the WTe_2 flake. The polarization of the incident laser was rotated from 0 to 360° by 10° increments using a polarization rotator, while an analyzer was set to only allow vertically polarized light to enter the spectrometer. Raman spectra were collected at each polarization for 3 acquisitions with a 20 s time per acquisition. The laser power was set to 0.5 mW at the sample to avoid any damage by heating. Following spectral collection, the (baseline corrected) integrated intensities under each peak were calculated to make the contour plots and polar plots in Figure 2c,d.

FMRFM Measurement and Signal Fitting. Our FMRFM performs locally and measures FMR at room temperature in a vacuum. The cantilever has a natural frequency of ∼18 kHz, spring constant of 0.2 N/m, and Q factor of ∼20000, resulting in a force detection sensitivity of 10^{-15} N/$Hz^{1/2}$. The $SmCo_5$ magnetic particle attached to the cantilever has a magnetic moment of ∼4 nemu. When an LM is on resonance, the local reduction of magnetization in an out-of-plane direction will generate a stray field, which will couple the altered magnetization to the magnetic tip, thus changing the cantilever oscillation amplitude and frequency. The change in cantilever oscillation is detected optically by laser fiber interferometry. Different LMs have different mode radii. For this microscopy study, we focus on n = 1 LM since it gives the highest spatial resolution. The n = 1 LM resonance peak is fit to a Lorentzian line shape, from which the peak position and peak height are extracted, which correspond to the resonance field $H_{r,1}$ and signal amplitude ΔA.

■ ASSOCIATED CONTENT

Supporting Information

The Supporting Information is available free of charge at https://pubs.acs.org/doi/10.1021/acs.nanolett.1c04237.

https://doi.org/10.1021/acs.nanolett.1c04237
Nano Lett. 2022, 22, 1115−1121

A description of raw data on WTe_2 thickness dependence, an FMRFM measurement on a second sample, an FMRFM measurement at different RF frequencies, a description of polarized Raman measurement result, and a detailed illustration of the impact of broken mirror reflection symmetries on the magnetic anisotropy (PDF)

AUTHOR INFORMATION

Corresponding Author

Guanzhong Wu − *Department of Physics, The Ohio State University, Columbus, Ohio 43210, United States;* orcid.org/0000-0001-6679-8332; Email: wu.2314@osu.edu

Authors

Dongying Wang − *Department of Physics, The Ohio State University, Columbus, Ohio 43210, United States;* orcid.org/0000-0002-9674-3532

Nishchhal Verma − *Department of Physics, The Ohio State University, Columbus, Ohio 43210, United States*

Rahul Rao − *Materials and Manufacturing Directorate, Air Force Research Laboratory, Wright-Patterson Air Force Base, Dayton, Ohio 45433, United States*

Yang Cheng − *Department of Physics, The Ohio State University, Columbus, Ohio 43210, United States*

Side Guo − *Department of Physics, The Ohio State University, Columbus, Ohio 43210, United States*

Guixin Cao − *Department of Physics, The Ohio State University, Columbus, Ohio 43210, United States*

Kenji Watanabe − *Research Center for Functional Materials, National Institute for Materials Science, Tsukuba 305-0044, Japan;* orcid.org/0000-0003-3701-8119

Takashi Taniguchi − *International Center for Materials Nanoarchitectonics, National Institute for Materials Science, Tsukuba 305-0044, Japan;* orcid.org/0000-0002-1467-3105

Chun Ning Lau − *Department of Physics, The Ohio State University, Columbus, Ohio 43210, United States;* orcid.org/0000-0003-2159-6723

Fengyuan Yang − *Department of Physics, The Ohio State University, Columbus, Ohio 43210, United States;* orcid.org/0000-0001-6921-1533

Mohit Randeria − *Department of Physics, The Ohio State University, Columbus, Ohio 43210, United States*

Marc Bockrath − *Department of Physics, The Ohio State University, Columbus, Ohio 43210, United States;* orcid.org/0000-0002-7000-1442

P. Chris Hammel − *Department of Physics, The Ohio State University, Columbus, Ohio 43210, United States*

Complete contact information is available at: https://pubs.acs.org/10.1021/acs.nanolett.1c04237

Notes

The authors declare no competing financial interest.

ACKNOWLEDGMENTS

This work was primarily supported by the Center for Emergent Materials: an NSF MRSEC under award number DMR-2011876 (G.W., N.V., Y.C,. S.G., F.Y., M.R., and P.C.H.). K.W. and T.T. acknowledge support from the Elemental Strategy Initiative conducted by the MEXT, Japan (JPMXP0112101001), and JSPS KAKENHI (19H05790, 20H00354, and 21H05233). D.W., G.C., and M.B. are supported by NSF under award DMR-2004801. CNL is supported by NSF under award DMR 2128945. We gratefully acknowledge N. Trivedi for insightful discussions. Fabrication and some characterization were performed in the Ohio State University NanoSystems Laboratory.

REFERENCES

(1) Dieny, B.; Chshiev, M. Perpendicular magnetic anisotropy at transition metal/oxide interfaces and applications. *Rev. Mod. Phys.* **2017**, *89* (2), 025008.

(2) Lee, K. S.; Lee, S. W.; Min, B. C.; Lee, K. J. Threshold current for switching of a perpendicular magnetic layer induced by spin Hall effect. *Appl. Phys. Lett.* **2013**, *102* (11), 112410.

(3) Carcia, P. F.; Meinhaldt, A. D.; Suna, A. Perpendicular Magnetic-Anisotropy in Pd/Co Thin-Film Layered Structures. *Appl. Phys. Lett.* **1985**, *47* (2), 178−180.

(4) Ikeda, S.; Miura, K.; Yamamoto, H.; Mizunuma, K.; Gan, H. D.; Endo, M.; Kanai, S.; Hayakawa, J.; Matsukura, F.; Ohno, H. A perpendicular-anisotropy CoFeB-MgO magnetic tunnel junction. *Nat. Mater.* **2010**, *9* (9), 721−724.

(5) Yang, H. X.; Chen, G.; Cotta, A. A. C.; N'Diaye, A. T.; Nikolaev, S. A.; Soares, E. A.; Macedo, W. A. A.; Liu, K.; Schmid, A. K.; Fert, A.; Chshiev, M. Significant Dzyaloshinskii-Moriya interaction at graphene-ferromagnet interfaces due to the Rashba effect. *Nat. Mater.* **2018**, *17* (7), 605−609.

(6) Zeper, W. B.; Greidanus, F. J. A. M.; Carcia, P. F. Evaporated Co/Pt Layered Structures for Magneto-Optical Recording. *Ieee Transactions on Magnetics* **1989**, *25* (5), 3764−3766.

(7) Brataas, A.; van Wees, B.; Klein, O.; de Loubens, G.; Viret, M. Spin insulatronics. *Phys. Rep.* **2020**, *885*, 1−27.

(8) Li, P.; Liu, T.; Chang, H. C.; Kalitsov, A.; Zhang, W.; Csaba, G.; Li, W.; Richardson, D.; DeMann, A.; Rimal, G.; Dey, H.; Jiang, J.; Porod, W.; Field, S. B.; Tang, J. K.; Marconi, M. C.; Hoffmann, A.; Mryasov, O.; Wu, M. Z. Spin-orbit torque-assisted switching in magnetic insulator thin films with perpendicular magnetic anisotropy. *Nat. Commun.* **2016**, *7*, 1−8.

(9) Tang, C.; Sellappan, P.; Liu, Y. W.; Xu, Y. D.; Garay, J. E.; Shi, J. Anomalous Hall hysteresis in Tm3Fe5O12/Pt with strain-induced perpendicular magnetic anisotropy. *Phys. Rev. B* **2016**, *94* (14), 140403.

(10) Soumah, L.; Beaulieu, N.; Qassym, L.; Carretero, C.; Jacquet, E.; Lebourgeois, R.; Ben Youssef, J.; Bortolotti, P.; Cros, V.; Anane, A. Ultra-low damping insulating magnetic thin films get perpendicular. *Nat. Commun.* **2018**, *9*, 1−6.

(11) Li, G.; Bai, H.; Su, J.; Zhu, Z. Z.; Zhang, Y.; Cai, J. W. Tunable perpendicular magnetic anisotropy in epitaxial Y3Fe5O12 films. *Apl. Materials* **2019**, *7* (4), 041104.

(12) Fu, J. B.; Hua, M. X.; Wen, X.; Xue, M. Z.; Ding, S. L.; Wang, M.; Yu, P.; Liu, S. Q.; Han, J. Z.; Wang, C. S.; Du, H. L.; Yang, Y. C.; Yang, J. B. Epitaxial growth of Y3Fe5O12 thin films with perpendicular magnetic anisotropy. *Appl. Phys. Lett.* **2017**, *110* (20), 202403.

(13) Lee, A. J.; Ahmed, A. S.; McCullian, B. A.; Guo, S. D.; Zhu, M. L.; Yu, S. S.; Woodward, P. M.; Hwang, J.; Hammel, P. C.; Yang, F. Y. Interfacial Rashba-Effect-Induced Anisotropy in Nonmagnetic-Material-Ferrimagnetic-Insulator Bilayers. *Phys. Rev. Lett.* **2020**, *124* (25), 257202.

(14) Tang, C.; Song, Q.; Chang, C. Z.; Xu, Y. D.; Ohnuma, Y.; Matsuo, M.; Liu, Y. W.; Yuan, W.; Yao, Y. Y.; Moodera, J. S.; Maekawa, S.; Han, W.; Shi, J. Dirac surface state-modulated spin dynamics in a ferrimagnetic insulator at room temperature. *Science Advances* **2018**, *4* (6), eaas8660.

(15) Wu, G. Z.; White, S. P.; Ruane, W. T.; Brangham, J. T.; Pelekhov, D. V.; Yang, F. Y.; Hammel, P. C. Local measurement of interfacial interactions using ferromagnetic resonance force microscopy. *Phys. Rev. B* **2020**, *101* (18), 184409.

(16) Liu, T.; Kally, J.; Pillsbury, T.; Liu, C. P.; Chang, H. C.; Ding, J. J.; Cheng, Y.; Hilse, M.; Engel-Herbert, R.; Richardella, A.; Samarth, N.; Wu, M. Z. Changes of Magnetism in a Magnetic Insulator due to Proximity to a Topological Insulator. *Phys. Rev. Lett.* **2020**, *125* (1), 017204.
(17) Li, P.; Wen, Y.; He, X.; Zhang, Q.; Xia, C.; Yu, Z. M.; Yang, S. Y. A.; Zhu, Z. Y.; Alshareef, H. N.; Zhang, X. X. Evidence for topological type-II Weyl semimetal WTe2. *Nat. Commun.* **2017**, *8*, 1−8.
(18) Lv, Y. Y.; Li, X.; Zhang, B. B.; Deng, W. Y.; Yao, S. H.; Chen, Y. B.; Zhou, J.; Zhang, S. T.; Lu, M. H.; Zhang, L.; Tian, M. L.; Sheng, L.; Chen, Y. F. Experimental Observation of Anisotropic Adler-Bell-Jackiw Anomaly in Type-II Weyl Semimetal WTe1.98 Crystals at the Quasiclassical Regime. *Phys. Rev. Lett.* **2017**, *118* (9), 096603.
(19) Shi, S.; Li, J.; Hsu, C.-H.; Lee, K.; Wang, Y.; Yang, L.; Wang, J.; Wang, Q.; Wu, H.; Zhang, W.; Eda, G.; Liang, G.; Chang, H.; Yang, H. Observation of the Out-of-Plane Polarized Spin Current from CVD Grown WTe2. *Adv. Quantum Technol.* **2021**, *4* (8), 2100038.
(20) Shi, S. Y.; Liang, S. H.; Zhu, Z. F.; Cai, K. M.; Pollard, S. D.; Wang, Y.; Wang, J. Y.; Wang, Q. S.; He, P.; Yu, J. W.; Eda, G.; Liang, G. C.; Yang, H. All-electric magnetization switching and Dzyaloshinskii-Moriya interaction in WTe2/ferromagnet heterostructures. *Nat. Nanotechnol.* **2019**, *14* (10), 945−949.
(21) Zhao, B.; Karpiak, B.; Khokhriakov, D.; Johansson, A.; Hoque, A. M.; Xu, X. G.; Jiang, Y.; Mertig, I.; Dash, S. P. Unconventional Charge-Spin Conversion in Weyl-Semimetal WTe2. *Adv. Mater.* **2020**, *32* (38), 2000818.
(22) Zhao, B.; Khokhriakov, D.; Zhang, Y.; Fu, H.; Karpiak, B.; Hoque, A. M..; Xu, X.; Jiang, Y.; Yan, B.; Dash, S. P. Observation of charge to spin conversion in Weyl semimetal WTe2 at room temperature. *Phys. Rev. Res.* **2020**, *2* (1), 013286.
(23) Fukami, S.; Anekawa, T.; Zhang, C.; Ohno, H. A spin-orbit torque switching scheme with collinear magnetic easy axis and current configuration. *Nat. Nanotechnol.* **2016**, *11* (7), 621−625.
(24) Kao, I.-H.; Muzzio, R.; Zhang, H.; Zhu, M.; Gobbo, J.; Weber, D.; Rao, R.; Li, J.; Edgar, J. H.; Goldberger, J. E.; Yan, J.; Mandrus, D. G.; Hwang, J.; Cheng, R.; Katoch, J.; Singh, S. Field-free deterministic switching of a perpendicularly polarized magnet using unconventional spin-orbit torques in WTe2. 2020, arXiv.https://arxiv.org/ftp/arxiv/papers/2012/2012.12388.pdf (accessed Jan 22, 2022).
(25) Shin, I.; Cho, W. J.; An, E.-S.; Park, S.; Jeong, H.-W.; Jang, S.; Baek, W. J.; Park, S. Y.; Yang, D.-H.; Seo, J. H.; Kim, G.-Y.; Ali, M. N.; Choi, S.-Y.; Lee, H.-W.; Kim, J. S.; Kim, S.; Lee, G.-H. Spin-orbit torque Switching in an All-Van der Waals Heterostructure. 2021, arXiv. https://arxiv.org/ftp/arxiv/papers/2102/2102.09300.pdf (accessed Jan 22, 2022).
(26) Gallagher, J. C.; Yang, A. S.; Brangham, J. T.; Esser, B. D.; White, S. P.; Page, M. R.; Meng, K. Y.; Yu, S. S.; Adur, R.; Ruane, W.; Dunsiger, S. R.; McComb, D. W.; Yang, F. Y.; Hammel, P. C. Exceptionally high magnetization of stoichiometric Y3Fe5O12 epitaxial films grown on Gd3Ga5O12. *Appl. Phys. Lett.* **2016**, *109* (7), 072401.
(27) Ali, M. N.; Xiong, J.; Flynn, S.; Tao, J.; Gibson, Q. D.; Schoop, L. M.; Liang, T.; Haldolaarachchige, N.; Hirschberger, M.; Ong, N. P.; Cava, R. J. Large, non-saturating magnetoresistance in WTe2. *Nature* **2014**, *514* (7521), 205−208.
(28) Tang, S. J.; Zhang, C. F.; Wong, D.; Pedramrazi, Z.; Tsai, H. Z.; Jia, C. J.; Moritz, B.; Claassen, M.; Ryu, H.; Kahn, S.; Jiang, J.; Yan, H.; Hashimoto, M.; Lu, D. H.; Moore, R. G.; Hwang, C. C.; Hwang, C.; Hussain, Z.; Chen, Y. L.; Ugeda, M. M.; Liu, Z.; Xie, X. M.; Devereaux, T. P.; Crommie, M. F.; Mo, S. K.; Shen, Z. X. Quantum spin Hall state in monolayer 1T′-WTe2. *Nat. Phys.* **2017**, *13* (7), 683.
(29) Kang, K. F.; Li, T. X.; Sohn, E.; Shan, J.; Mak, K. F. Nonlinear anomalous Hall effect in few-layer WTe2. *Nat. Mater.* **2019**, *18* (4), 324.
(30) MacNeill, D.; Stiehl, G.; Guimaraes, M.; Buhrman, R.; Park, J.; Ralph, D. Control of spin−orbit torques through crystal symmetry in WTe 2/ferromagnet bilayers. *Nat. Phys.* **2017**, *13* (3), 300.
(31) MacNeill, D.; Stiehl, G. M.; Guimaraes, M. H. D.; Reynolds, N. D.; Buhrman, R. A.; Ralph, D. C. Thickness dependence of spin-orbit torques generated by WTe2. *Phys. Rev. B* **2017**, *96* (5), 054450.
(32) Yang, F. Y.; Hammel, P. C. FMR-driven spin pumping in Y3Fe5O12-based structures. *J. Phys. D: Appl. Phys.* **2018**, *51* (25), 253001.
(33) Lee, I.; Obukhov, Y.; Xiang, G.; Hauser, A.; Yang, F.; Banerjee, P.; Pelekhov, D. V.; Hammel, P. C. Nanoscale scanning probe ferromagnetic resonance imaging using localized modes. *Nature* **2010**, *466* (7308), 845.
(34) Adur, R.; Du, C.; Manuilov, S. A.; Wang, H.; Yang, F.; Pelekhov, D. V.; Hammel, P. C. The magnetic particle in a box: Analytic and micromagnetic analysis of probe-localized spin wave modes. *J. Appl. Phys.* **2015**, *117* (17), 17E108.
(35) Du, C.; Lee, I.; Adur, R.; Obukhov, Y.; Hamann, C.; Buchner, B.; McCord, J.; Pelekhov, D. V.; Hammel, P. C. Imaging interfaces defined by abruptly varying internal magnetic fields by means of scanned nanoscale spin wave modes. *Phys. Rev. B* **2015**, *92* (21), 214413.
(36) Lee, I.; Obukhov, Y.; Hauser, A. J.; Yang, F. Y.; Pelekhov, D. V.; Hammel, P. C. Nanoscale confined mode ferromagnetic resonance imaging of an individual Ni81Fe19 disk using magnetic resonance force microscopy (invited). *J. Appl. Phys.* **2011**, *109* (7), 07D313.
(37) Song, Q. J.; Wang, H. F.; Xu, X. L.; Pan, X. C.; Wang, Y. L.; Song, F. Q.; Wan, X. G.; Dai, L. The polarization-dependent anisotropic Raman response of few-layer and bulk WTe2 under different excitation wavelengths. *Rsc Adv.* **2016**, *6* (105), 103830−103837.
(38) Tserkovnyak, Y.; Brataas, A.; Bauer, G. E. Enhanced Gilbert damping in thin ferromagnetic films. *Phys. Rev. Lett.* **2002**, *88* (11), 117601.
(39) Wu, G. Z.; Cheng, Y.; Guo, S. D.; Yang, F.; Pelekhov, D.; Hammel, P. C. Nanoscale imaging of Gilbert damping using signal amplitude mapping. *Appl. Phys. Lett.* **2021**, *118* (4), 042403.
(40) Lee, A. J.; Ahmed, A. S.; Flores, J.; Guo, S. D.; Wang, B. B.; Bagues, N.; McComb, D. W.; Yang, F. Y. Probing the Source of the Interfacial Dzyaloshinskii-Moriya Interaction Responsible for the Topological Hall Effect in Metal/Tm3Fe5O12 Systems. *Phys. Rev. Lett.* **2020**, *124* (10), 107201.
(41) Banerjee, S.; Rowland, J.; Erten, O.; Randeria, M. Enhanced Stability of Skyrmions in Two-Dimensional Chiral Magnets with Rashba Spin-Orbit Coupling. *Physical Review X* **2014**, *4* (3), 031045.
(42) Wang, Y. J.; Liu, E. F.; Liu, H. M.; Pan, Y. M.; Zhang, L. Q.; Zeng, J. W.; Fu, Y. J.; Wang, M.; Xu, K.; Huang, Z.; Wang, Z. L.; Lu, H. Z.; Xing, D. Y.; Wang, B. G.; Wan, X. G.; Miao, F. Gate-tunable negative longitudinal magnetoresistance in the predicted type-II Weyl semimetal WTe2. *Nat. Commun.* **2016**, *7* (1), 1−6.
(43) Wu, Y. Y.; Zhang, S. F.; Zhang, J. W.; Wang, W.; Zhu, Y. L.; Hu, J.; Yin, G.; Wong, K.; Fang, C.; Wan, C. H.; Han, X. F.; Shao, Q. M.; Taniguchi, T.; Watanabe, K.; Zang, J. D.; Mao, Z. Q.; Zhang, X. X.; Wang, K. L. Neel-type skyrmion in WTe2/Fe3GeTe2 van der Waals heterostructure. *Nat. Commun.* **2020**, *11* (1), 1−6.
(44) Wang, D. Y.; Che, S.; Cao, G. X.; Lyu, R.; Watanabe, K.; Taniguchi, T.; Lau, C. N.; Bockrath, M. Quantum Hall Effect Measurement of Spin-Orbit Coupling Strengths in Ultraclean Bilayer Graphene/WSe2 Heterostructures. *Nano Lett.* **2019**, *19* (10), 7028−7034.
(45) Zhao, Y. F.; Liu, H. W.; Yan, J. Q.; An, W.; Liu, J.; Zhang, X.; Wang, H. C.; Liu, Y.; Jiang, H.; Li, Q.; Wang, Y.; Li, X. Z.; Mandrus, D.; Xie, X. C.; Pan, M. H.; Wang, J. Anisotropic magnetotransport and exotic longitudinal linear magnetoresistance in WTe2 crystals. *Phys. Rev. B* **2015**, *92* (4), 041104.

https://doi.org/10.1021/acs.nanolett.1c04237
Nano Lett. 2022, 22, 1115−1121